Sustained axisymmetric intrusions in a rotating system

M. Ungarish[a], C. G. Johnson[b,*], A. J. Hogg[c]

[a] *Dept. Computer Science, Technion, Haifa 32000, Israel*
[b] *Centre for Nonlinear Dynamics and School of Mathematics, University of Manchester, UK*
[c] *Centre for Environmental & Geophysical Flows, School of Mathematics, University of Bristol, UK*

Abstract

We analyse the effects of rotation on the propagation of an axisymmetric intrusion through a linearly stratified ambient fluid, arising from a sustained source at the level of neutral buoyancy. This scenario occurs during the horizontal spreading of a large volcanic ash cloud, which occurs after the plume has risen to its neutral buoyancy level. A simple and well-accepted approximation for the flow at late times is that inertial effects are negligible. This leads to a lens-shaped intrusion governed by a balance between Coriolis accelerations and horizontal pressure gradients, with a radius scaling with time as $r_N \sim t^{1/3}$. However, we show using shallow-layer model that inertial forces cannot be neglected until significant times after the beginning of the influx. These inertial forces result in the flow forming two distinct domains, separated by a moving hydraulic jump: an outer 'head' region in which the radial velocity and thickness vary with time, and a thinner 'tail' region in which the flow is steady. Initially, the flow expands rapidly and this tail region occupies most of the flow. After about one half-revolution of the system, Coriolis accelerations halt the advance of the front, and the hydraulic jump separating the two regions propagates back towards the source of the intrusion. Only after approximately one and a half rotations of the system does inertia become insignificant and the Coriolis lens solution, with $r_N \sim t^{1/3}$, become established. Importantly, this means that neither inertia nor Coriolis accelerations can be neglected when modelling intrusions from volcanic eruptions. We exploit the two-region flow structure to construct a new hybrid model, comprising just two ordinary differential equations for the intrusion radius and location of the hydraulic jump. This hybrid model is much simpler than the shallow-layer model, but nonetheless accurately predicts flow properties such as the intrusion radius at all stages of motion, without requiring fitted or adjustable parameters.

1. Introduction

Large-scale, density-driven flows, which are predominantly horizontal, are common in environmental and geophysical settings. They arise due to compositional differences between the intruding fluid and the surrounding ambient, which perturb the pressure distribution, generate horizontal pressure gradients and give rise to the motion. However the effects of the earth's rotation can influence the flow; in particular, rotation-induced forces tend to oppose the gravitational spreading [1] and these effects may be most pronounced for large-scale and long-lived phenomena. In this contribution, we analyse the motion due to a sustained influx of fluid at its height of neutral buoyancy within a continuously stratified ambient. Specific examples include intrusions within stratified lakes [2] and the atmospheric dispersion of volcanic ash clouds [3]. The latter has been a recent focus of much research activity given the potential for catastrophic effects of ash on air-

*Corresponding author
Email addresses: unga@cs.technion.ac.il (M. Ungarish), chris.johnson@manchester.ac.uk (C. G. Johnson), a.j.hogg@bristol.ac.uk (A. J. Hogg)

craft engines and the closure of airspace to mitigate this hazard [4, 5]. Volcanic plumes rise from their source, mixing with the atmosphere, until their bulk density matches that of the surroundings. They then intrude, predominantly horizontally, at this level of neutral buoyancy with their motion driven at least in part by the perturbation they cause to the background distribution of density in the atmosphere [3].

In this study we investigate the effects of rotation on a sustained intrusion in a continuously stratified ambient, which is otherwise quiescent, and we analyse its radial motion as it spreads away from its source. Rotation slows and inhibits the radial motion and, in the absence of dissipative processes, the flow is expected to approach a state of geostrophic balance in which the gravitational and Coriolis forces are in equilibrium [1]. This geostrophic balance has been studied in a different scenario, in which a volume of relatively dense fluid is released instantaneously within a uniform, less dense ambient [6, 7]. In this situation, the dense fluid eventually forms a basal, static 'lens', although due to its own inertia, the flow may initially overshoot the final state before recovering to it [7, 8]. Similar behaviour occurs in flows in continuously stratified environments [9], with the final state, after many rotations, exhibiting an ellipsoidal shape [8], which continues to grow slowly if fed by a sustained source [10, 11, 12]. Continuously stratified fluids support the propagation of internal waves, and while these can significantly influence the transient behaviour of intrusions [9], they do not alter the geostrophic balance underlying this final ellipsoidal shape.

Recent studies have revealed that, in the absence of rotation, sustained axisymmetric flows evolve differently from their two-dimensional counterparts; rather than evolving to a self-similar state in which representative thickness and velocity fields exhibit the same temporal dependence throughout the entire current, there are different dependencies in the tail of the current from at its front. This implies that straightforward scaling, which is so often useful for this kind of motion, is misleading and leads to incorrect predictions of the behaviour of sustained axisymmetric flows [3]. In this study, our contributions are twofold. Firstly, we develop a shallow layer model for the thickness and depth-averaged radial and angular velocities of a sustained intrusion in the regime where the inertia of the flow is initially dynamically important, but progressively wanes as the effects of rotation begin to play a role. This progression from inertia- to rotation-dominated spreading is particularly relevant to ash clouds arising from large sustained volcanic eruptions, but to our knowledge no experimental data are available for this configuration. The results from our shallow-layer model reveal how the lens-like solution emerges even from a flow that is initially dominated by inertia (i.e. a flow with an initially large Rossby number). We show that it is misleading to treat the flow as lens-like throughout its evolution, and that for a significant duration the flow instead exhibits a steady tail attached to the source with a time dependent frontal region. Secondly, we present a simplified model for the propagation of the intrusion, which captures the transition from an inertially-dominated flow to one in geostrophic balance. For flows arising from instantaneous slumps of dense fluid in a rotating ambient of uniform density, it has been demonstrated that reduced 'integral' models capture the key temporal dependencies in the flow (see, for example, [13] and [8]). These models are useful because they permit rapid computation of a flow state without the need for the integration of the more complete shallow water equations. However, this 'box' model approach is inappropriate for these sustained axisymmetric intrusions. Instead we generalise the approach of Ungarish *et al.* [14] to develop a hybrid model that encompasses the effects of rotation. This is a non-trivial extension because Coriolis processes arrest the flow and lead progressively to geostrophic balance, features that are absent from the non-rotating counterpart. We show that this new hybrid model is capable of accurately reproducing the behaviour predicted by the more

complete governing equations and that it is therefore a tool of considerable practical importance.

The paper is structured as follows. First, we formulate the problem, identify the key dimensionless parameters that characterise the effects of rotation and compute solutions of the shallow-layer model numerically (§2). We further demonstrate how the lens-like solution is approached progressively in time, a calculation that requires matched expansions between the bulk of the flow and the frontal region. In §3 we develop the hybrid model for these flows, showing how it simplifies and yet accurately captures the dynamics. We present results and give interpretations in §4, before summarising our findings in §5.

2. Shallow layer model

We analyse the radial propagation of relatively shallow intrusions through a continuously stratified, rotating environment (figure 1), which is characterised by two inverse timescales: an angular velocity Ω, and a buoyancy frequency, $\mathcal{N}$, defined by $\mathcal{N}^2 = -g(d\rho/dz)/\rho_c$, where z is the vertical coordinate, g is the acceleration due to gravity, ρ is the ambient fluid density and ρ_c is the density of the intruding fluid. The dimensionless Coriolis parameter is defined by

$$\mathcal{L} = \frac{\Omega}{\mathcal{N}}, \tag{1}$$

and characterises the strength of the rotation [*cf.* 8]. For typical atmospheric conditions, where $\mathcal{N} \approx 10^{-2}\mathrm{s}^{-1}$ and $\Omega \approx 10^{-5}\mathrm{s}^{-1}$, we therefore anticipate that $\mathcal{L} = O(10^{-3})$ but we shall consider solutions for a wide range of values.

The motion of intrusions through a surrounding fluid of constant buoyancy frequency occurs symmetrically about the level of neutral buoyancy and is driven by the radial gradients of the pressure field due to the perturbation to the background stratification. Intrusions through a continuously stratified environment may be modelled using a shallow layer model, in which vertical fluid accelerations are assumed negligible (see, for example, [8] and the references therein). This neglects the generation of internal waves and only resolves the predominantly horizontal motion about the level of neutral buoyancy. This assumption that internal waves do not significantly alter the dynamics of axisymmetric intrusions continuously supplied by a buoyant plume is supported by the experiments of Ansong & Sutherland [15], in which only $\sim 4\%$ of the flow energy was transferred to internal waves. This contrasts with other flows, such as intrusions generated by a sudden collapse of mixed fluid, in which internal waves can play a more significant role [9]. Large-scale experiments may be necessary to determine conclusively how internal waves and other disturbances to the ambient stratification interact with the volcanic intrusions that motivate this study[3].

In this investigation, we focus on flows due to a sustained volume flux of fluid $2\pi Q$ at an inflow radius $r = r_i$ and we form axisymmetric governing equations in terms of cylindrical polar coordinates with the symmetry axis aligned with gravity, for the half thickness, h, and the depth-averaged radial and angular velocities, u and ω, respectively. The dependent variables are rendered dimensionless by the lengthscale $(Q/(2\mathcal{N}))^{1/3}$, timescale $\mathcal{N}^{-1}$, radial velocity scale $(Q\mathcal{N}^2/2)^{1/3}$ and angular velocity scale Ω. The dimensionless equations are then given by

$$\frac{\partial h}{\partial t} + \frac{1}{r}\frac{\partial}{\partial r}(rhu) = 0, \tag{2}$$

$$\frac{\partial u}{\partial t} + \frac{1}{2}\frac{\partial}{\partial r}(u^2 + h^2) = \mathcal{L}^2\omega r(2+\omega), \tag{3}$$

$$r\frac{\partial \omega}{\partial t} + u\frac{\partial}{\partial r}(\omega r) = -u(2+\omega). \tag{4}$$

The derivation of these equations can be found in [8] (§13.1; note that the intrusion corresponds to $S = 1$ in that formulation). The 'Coriolis acceleration' terms on the right-hand side of these equations are due to the background rotation of the system, and it is the effect of these terms that is the focus of this investigation. It is insightful to rearrange (2)–(4) into an expression of energy conser-

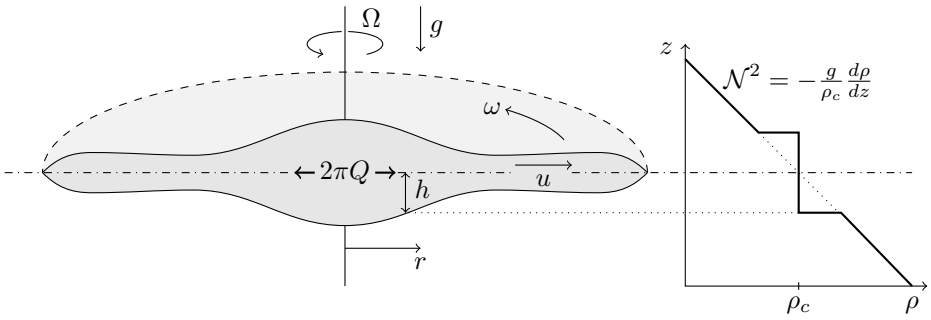

Figure 1: Schematic of the rotating axisymmetric intrusions under consideration, illustrating the main parameters describing the system: the volume flux $2\pi Q$ at the source, the rotation rate of the system, Ω, and the stratification of the background atmosphere, parametrised by $\mathcal{N}$. Within the intrusion the density is constant ($\rho = \rho_c$) and the flow is described by the half-thickness h, radial velocity u and angular velocity ω, each functions of the radial distance r and time t.

vation,

$$\frac{\partial}{\partial t}\left(\frac{h}{2}\left(u^2+\mathcal{L}^2r^2\omega^2\right)+\frac{h^3}{6}\right) + \frac{1}{r}\frac{\partial}{\partial r}\left(\frac{ruh}{2}\left(u^2+\mathcal{L}^2r^2\omega^2+h^2\right)\right)=0, \quad (5)$$

which reflects a balance between the rate of change of the kinetic and potential energies, their advection and the work done by the hydrostatic pressure. The governing equations (2)–(4) form a hyperbolic system with dimensionless characteristic speeds, $c, c_\pm$, given by

$$c = u \qquad \text{and} \qquad c_\pm = u \pm h. \quad (6)$$

On the characteristic $\mathrm{d}r/\mathrm{d}t = u$, we have

$$r\frac{\mathrm{d}\omega}{\mathrm{d}r} = -2(1+\omega), \quad (7)$$

and upon integrating this equation, we find that ω adopts the steady distribution

$$\omega = -1 + B_0/r^2, \quad (8)$$

where B_0 is a constant of order unity, which is determined from the boundary conditions. From (8) we note that the intrusion is counter rotating ($\omega \approx -1$) far from source.

The shallow water system (2)–(4) is subject to initial and boundary conditions. At the front of the current $r = r_N$ (values at the front, or nose, are denoted with the subscript N) we apply the kinematic condition $\mathrm{d}r_N/\mathrm{d}t = u_N$, along with a dynamic boundary condition,

$$u_N = \frac{F}{\sqrt{2}}h_N, \quad (9)$$

where F is of order unity. When the thickness of the intrusion is much smaller than the height of the ambient fluid, as assumed here, F is well approximated by a constant, with a practical value of 1.19 [8, 14]. At the source $r = r_i$, there is a sustained influx of material, given by

$$ruh = 1 \qquad \text{at} \qquad r = r_i. \quad (10)$$

This material exits with angular velocity ω_i in the rotating frame, so that pdf

$$\omega = \omega_i \qquad \text{at} \qquad r = r_i, \quad (11)$$

which, from (8), sets $B_0 = (\omega_i + 1)r_i^2$. (In the simulations that follow we further assume that the fluid at source rotates with the rotating frame, so that $\omega_i = 0$ and $B_0 = r_i^2$.) Finally, if the source is supercritical at $r = r_i$, we must impose a additional second boundary condition, which can be given by specifying a source energy flux per unit mass flux (see (5))

$$u_i^2 + \mathcal{L}_i^2 r_i^2 \omega_i^2 + h_i^2 = E \quad (12)$$

or a source Froude number $Fr_i = u_i/h_i$.

In spite of the apparent simplicity of the shallow layer equations, the solution of a practical problem may encounter various difficulties such as internal jumps in the

flow state that manifest themselves as discontinuities in the dependent variables. Additionally there are complications as the symmetry axis is approached due to the coordinate singularity there. In general sophisticated numerical solvers must be used for integrating the governing partial differential equations, as detailed below. Simplified solutions play an important role in revealing the dynamic processes and in making rapid calculations of the state of the flow.

2.1. Steady states

We first analyse steady solutions to the shallow-water model (2)–(4), noting that these play a vital role in in both time-dependent solutions (§2.2) and in the construction of our simplified hybrid model (§3). In a steady state, we deduce from (2) that the dimensionless radial mass flux is constant and given by

$$hur = 1. \tag{13}$$

Furthermore, from the expression of angular momentum conservation (4), provided the radial velocity is non-vanishing, (8) and (11) imply

$$\omega = -1 + \frac{B_0}{r^2}. \tag{14}$$

Finally, from the expression of energy conservation (5) and the constant radial mass flux (13), we find

$$\frac{\partial}{\partial r}\left(u^2 + \mathcal{L}^2\omega^2 r^2 + h^2\right) = 0, \tag{15}$$

which on integration yields

$$h^2 + u^2 = C_0^2 - \mathcal{L}^2\left(r^2 + \frac{B_0^4}{r^2}\right). \tag{16}$$

The constant C_0^2 is prescribed by the boundary conditions h_i, u_i at the inner radius r_i,

$$C_0^2 = h_i^2 + u_i^2 + \mathcal{L}^2\left(r_i^2 + \frac{B_0^4}{r_i^2}\right). \tag{17}$$

Further simplifying (16) using (13), we obtain separate quadratic equations for u^2 (and h^2), which are real-valued for $r_i \le r \le r_{\max}$, where $r_{\max}$ is defined below. These are given by

$$u^2 = \frac{1}{2}\left[D^2 + \sqrt{D^4 - 4/r^2}\right], \tag{18}$$

$$h^2 = \frac{1}{2}\left[D^2 - \sqrt{D^4 - 4/r^2}\right] = \frac{2}{D^2r^2 + \sqrt{(D^2r^2)^2 - 4r^2}}, \tag{19}$$

where the latter form avoids cancellation errors when r is large [see also 16]. Here,

$$D^2 = D^2(r) = C_0^2 - \mathcal{L}^2\left(r^2 + \frac{B_0^4}{r^2}\right). \tag{20}$$

Equation (16) admits also another solution for u^2 and h^2, in which the sign of the square roots is swapped; but this solution, which corresponds to subcritical motion, is not realised in time-dependent flows because it is not compatible with the boundary condition at the flow front (9).

The solution $h(r), u(r), \omega(r)$ given by (14), (18) and (19) is analytical and exact. The non-rotating case is recovered by setting $\mathcal{L} = 0$ and because in that case $D^2 = C_0^2$, the solutions of (18) and (19) are real-valued for all $r > r_i$ (i.e. $r_{\max}$ is unbounded). In this non-rotating case, h decays monotonically at large r, while u increases to the asymptote C_0 [14].

For the rotating case $\mathcal{L} > 0$ the behaviour is qualitatively different. We see from (20) that D^2 decreases and becomes negative for sufficiently large r, and therefore, in the rotating case, the domain of solution is restricted to $r < r_{\max}$ by the requirement that the square roots in (18) and (19) are real-valued, i.e., $D^2 \ge 2/r$. For $\mathcal{L} \ll 1$ (the regime expected in atmospheric flows) we evaluate $D^2(r_{max}) = 2/r_{max}$, and obtain

$$r_{\max} = \frac{C_0}{\mathcal{L}}\left(1 - \frac{\mathcal{L}}{C_0^3}\right) + \ldots, \tag{21}$$

$$u(r_{\max}) = h(r_{\max}) = \left(\frac{\mathcal{L}}{C_0}\right)^{1/2}\left(1 + \frac{1}{2}\frac{\mathcal{L}}{C_0^3}\right) + \ldots. \tag{22}$$

The radius $r_{\max}$ is the maximum potential domain of influence of the inertia influxed by the source, and is the radius at which the flow becomes critical ($c_- = 0$). Since

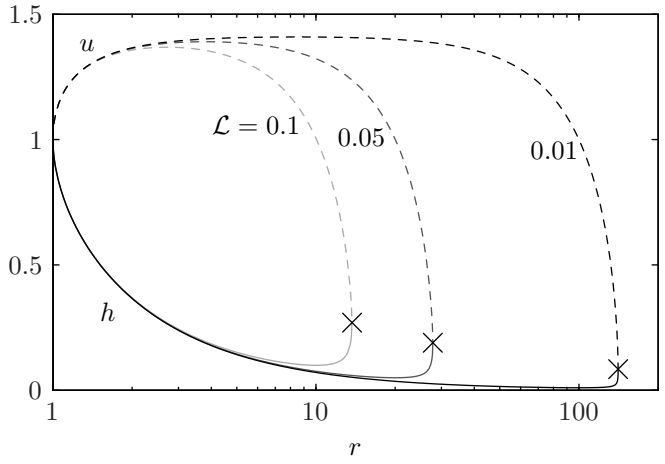

Figure 2: Flow half-thickness h (solid line) and radial velocity u (dashed line) as functions of radius r, for $\mathcal{L} = 0.01$, 0.05 and 0.1. The crosses indicate the small-$\mathcal{L}$ asymptotic approximations $r_{\max}$ and $u(r_{\max}) = h(r_{\max})$, given by (21) and (22). Here $r_i = u_i = h_i = 1$, $\omega_i = 0$.

the constant C_0 is of order of unity and $\mathcal{L} \ll 1$, (21) implies this domain of steady evolution may be extensive. On the other hand, at a sufficiently large radius the effects of rotation become dominant, even when $\mathcal{L} \ll 1$.

Typical profiles of h and u are shown in figure 2. In presence of Coriolis effects, h and u in the tail acquire a non-monotonic behaviour with r. For small $\mathcal{L}$, h decreases with r for most of the domain, while u increases gently to a maximum of about C_0. Close to $r_{\max}$, the trend is inverted. The crosses on each line in figure 2 are the approximations (21)–(22) for the corresponding value of $\mathcal{L}$, which show excellent agreement for $\mathcal{L} \leq 0.1$.

2.2. Temporal evolution: numerical computations

Having found steady solutions to the governing shallow layer equations (2)–(4), we now use numerical techniques to find time-dependent solutions. To do this we first rearrange the system into flux conservative form [17] and define a new radial variable rescaling the flow domain $[r_i, r_N]$ to the unit interval [18]. We then discretise the flow domain spatially using the non-oscillatory semi-discrete formulation of [19]. The shock-capturing property of this scheme means that the conservation of mass and momentum at jumps is automatically enforced. At the current nose, the kinematic boundary condition $\mathrm{d}r_N/\mathrm{d}t = u(r_N, t)$ determines the evolution of $r_N(t)$. The dynamic boundary condition applied at the nose is given by (9) when the current is radially advancing ($\mathrm{d}r_N/\mathrm{d}t > 0$). We apply this condition by augmenting the system of equations obtained from the discretisation of the flow domain with two additional ODEs, corresponding to the (9) (rewritten as $\mathrm{d}/\mathrm{d}t(u_N/h_N) = 0$) and to the equation satisfied on the forward-moving (+) characteristic at the nose. Together these specify the time evolution of $h_N(t)$ and $u_N(t)$ in terms of h, u, $\partial h/\partial r$ and $\partial u/\partial r$, evaluated at $r = r_N$. When the current nose is retreating ($\mathrm{d}r_N/\mathrm{d}t < 0$), the dynamic condition (9) can no longer be justified [8], and the appropriate boundary condition at the nose is that the boundary moves at the same speed as the c_+ characteristic, specified by setting $h_N(t) = 0$. We integrate the system of equations arising from the spatial discretisation of the flow domain, along with those for $h_N(t)$, $u_N(t)$ and $r_N(t)$, using a second-order Runge-Kutta method, with a CFL number of 1/4.

A typical numerical solution is plotted in figure 3. The flow initially expands radially and comprises two distinct regions: a time-dependent frontal region and a steady tail (figure 3a). These regions are connected by a shock, the radial location of which we denote by $r_1(t)$. This two-region solution structure is observed in the absence of rotation [14, 3], reflecting the relative unimportance of Coriolis accelerations relative to inertial times in the initial stages of the flow. The form of the steady tail region is influenced by the Coriolis accelerations in rotating flows, as detailed above. Though Coriolis accelerations influence the steady tail (§2.1), they have a more significant effect on the advancing flow front, slowing the radial advance of the current and eventually causing it to stop. This results in a second phase of motion (figure 3b) in which inertial overshoot causes the current radius to decrease with time (a similar overshoot was observed by [7] in axisymmetric rotating

gravity currents through an unstratified ambient). In this phase of motion the location of the shock separating the two flow regions also rapidly retreats towards the origin, due to continued outward flow within the tail region reaching the arrested or retreating flow head. The mechanism for this counter-intuitive motion of the shock is described in more detail in §3.3. After the initial stages of motion, the retreat of the shock means that the time-dependent frontal head region occupies all but a small region of the flow close to the origin, and this region adopts a rounded 'blunt-nosed' shape (figure 3c). The flow is then controlled by a balance between Coriolis accelerations and horizontal pressure gradients due to variations in the intrusion thickness. Although slowly-decaying inertial oscillations persist in the intrusion, resulting in alternate phases of advance and retreat of the current nose (figure 3d), at late times the flow approaches a self-similar rounded lens-like shape, and the current grows both in radius and in thickness (figure 3c). We now examine how this late-time similarity behaviour becomes established.

2.3. The Coriolis lens

Instantaneous releases of dense fluid within a rotating environment of uniform density adopt a convex lens shape in which the radial velocity vanishes [6]. A similar shape arises in intrusions through a stratified ambient [8], and also when the flow is due to a sustained flux of fluid [11, 16], though in this latter case the dimensions of this shape grow with time. Previous studies have not shown how the motion transitions from its inertially-dominated state at relatively early times to the Coriolis-dominated states at relatively late times, although it is evident from our numerical computations that there is a progressive evolution from one state to another. Here we demonstrate analytically how the Coriolis lens emerges from the governing equations as the inertial effects become progressively weaker.

First we note from (8) that when $r \gg 1$, the angular velocity $\omega = -1 + \ldots$ and so, far from the source, the current is counter-rotating to leading order in the rotating frame of reference. To analyse the ensuing motion it is convenient to write the independent variable as $y = r/r_N$ and to write the dependent variables as

$$h = \mathcal{L} r_N H(y,t) \qquad \text{and} \qquad u = \dot{r}_N U(y,t), \tag{23}$$

where a dot denotes differentiation with respect to time. In terms of these variables the governing equations become

$$H + \frac{r_N}{\dot{r}_N}\frac{\partial H}{\partial t} - y\frac{\partial H}{\partial y} + \frac{1}{y}\frac{\partial}{\partial y}\left(yUH\right) = 0, \tag{24}$$

$$\frac{1}{\mathcal{L}^2}\left(\frac{\ddot{r}_N}{r_N}U + \frac{\dot{r}_N^2}{r_N^2}U + \frac{r_N}{\dot{r}_N}\frac{\partial U}{\partial t} + \frac{\dot{r}_N^2}{r_N^2}(U-y)\frac{\partial U}{\partial y}\right) + \frac{1}{2}\frac{\partial}{\partial y}\left(H^2 + y^2\right) = 0. \tag{25}$$

The kinematic and dynamic conditions at the front of the current become

$$U(1) = 1 \qquad \text{and} \qquad \dot{r}_N = r_N \mathcal{L}\frac{F}{\sqrt{2}}H(1). \tag{26a,b}$$

Additionally, the requirement for a sustained volume flux at the source demands $\mathcal{L} r_N^2 \dot{r}_N y U H \to 1$ as $y \to 0$, where we have assumed that the radial position of the front far exceeds the radius of the source ($r_i/r_N \ll 1$).

We construct an asymptotic solution for the flow in regime $\mathcal{L}t \gg 1$, where Coriolis effects dominate. On the assumption that $\dot{r}_N t/r_N = O(1)$ and $\ddot{r}_N t^2/r_N = O(1)$, we deduce from (25) that

$$\frac{\partial}{\partial y}\left(H^2 + y^2\right) = 0, \tag{27}$$

i.e. that the depth-integrated pressure field, corrected for rotational (centrifugal) effects, is constant to leading order. From (27) we find that

$$H = \left(A^2 - y^2\right)^{1/2} + O((\mathcal{L}t)^{-2}), \tag{28}$$

where $A(t)$ is to be determined. On substitution of (28) in the equation for mass conservation (24) and integrating, we find that

$$U = \frac{A\dot{A} r_N/\dot{r}_N + A^2}{y} + \frac{A_1}{(A^2 - y^2)^{1/2} y}, \tag{29}$$

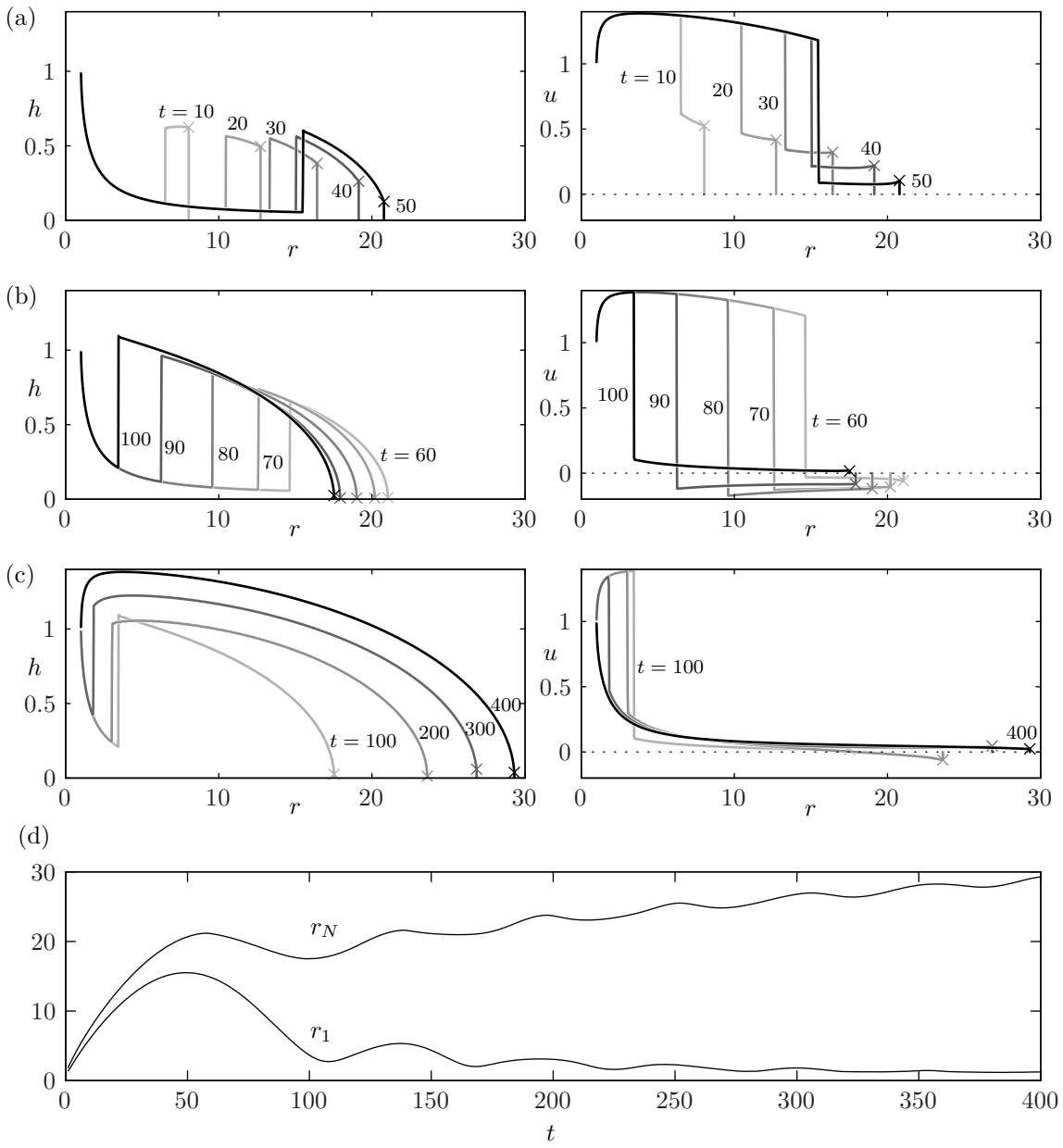

Figure 3: A numerical solution of the shallow layer model at $\mathcal{L} = 0.05$, $F = 1.19$, $r_i = h_i = u_i = 1$, $\omega_i = 0$. In panels (a)–(c) the flow half-thickness h (left panels) and the radial velocity u (right panels) are plotted as functions of the radial distance at various times. The cross indicates the values at the current nose. In panel (d), the radial position of the current nose r_N and radial position of the shock r_1 are plotted as functions of time.

where A_1 is another constant of integration, to be determined. At the front of the current ($y = 1$), the dynamic boundary condition (26b) becomes

$$\left(A^2 - 1\right)^{1/2} = \frac{1}{\mathcal{L}t}\frac{\dot{r}_N t}{r_N}\frac{\sqrt{2}}{F}. \tag{30}$$

Thus $A = 1$ to leading order and, from (28), the leading-order shape of the current is an oblate spheroid. However, this condition implies that the flow thickness vanishes to leading order at the front, from which (26b) implies that the propagation velocity of the front $\dot{r}_N$ is zero. This is inconsistent with a propagating current, and with the leading order solution for the velocity given by (29). We must therefore adopt a different asymptotic formulation to capture the evolution; while it is possible for the leading order expressions for the height and velocity fields, given by (28) and (29), to represent the flow dynamics within the bulk of current, they are inappropriate in a small region near the front.

We thus write a different asymptotic description of the velocity and thickness in the frontal region, and match this to the bulk flow. Denoting $\delta = (\mathcal{L}t)^{-2} \ll 1$, we deduce from (26a,b) that close to the front $U = O(1)$ and $H = O(\delta^{1/2})$, and then from (25), the distinguished scaling for the width of the frontal boundary layer is $(1 - y) = O(\delta)$. In terms of rescaled variables,

$$y = 1 - \delta Y, \qquad H = \delta^{1/2}\overline{H} \qquad \text{and} \qquad U = \overline{U}, \tag{31}$$

we find that to leading order in δ, mass conservation is given by

$$\frac{\partial \overline{H}}{\partial Y} - \frac{\partial}{\partial Y}\left(\overline{H}\,\overline{U}\right) = 0, \tag{32}$$

while the balance of momentum is

$$-\frac{t^2\dot{r}_N^2}{r_N^2}\left(\overline{U} - 1\right)\frac{\partial \overline{U}}{\partial Y} - \frac{1}{2}\frac{\partial}{\partial Y}\left(\overline{H}^2 - 2Y\right) = 0. \tag{33}$$

These are subject to boundary conditions at the front ($Y = 0$), $\overline{U} = 1$ and $\overline{H} = (t\dot{r}_N/r_N)(\sqrt{2}/F)$. The leading order solution within the frontal boundary layer is then given by

$$\overline{U} = 1 \qquad \text{and} \qquad \overline{H} = \left(2Y + \left(\frac{t\dot{r}_N}{r_N}\frac{\sqrt{2}}{F}\right)^2\right)^{1/2}. \tag{34}$$

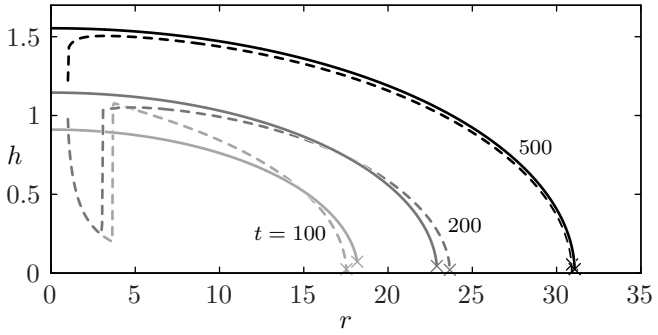

Figure 4: The composite solution (37) (solid curve), compared to shallow water model results (dashed curves). Model parameters are as for figure 3, namely $\mathcal{L} = 0.05$, $F = 1.19$, $r_i = h_i = u_i = 1$, $\omega_i = 0$.

Matching these expressions to the flow fields within the bulk ($Y \gg 1$), we find that $A = 1$ and $A_1 = 0$. Finally we impose the flux conservation at the source and this demands

$$\mathcal{L}r_N^2\dot{r}_N = 1 \qquad \text{and so} \qquad r_N = (3t/\mathcal{L})^{1/3}. \tag{35}$$

In terms of the original variables, the composite solution (obtained by summing the outer and inner solutions, (28) and (34), and subtracting the form in the matching region $\bar{H} = (2Y)^{1/2}$) is

$$h(r,t) = \mathcal{L}r_N(t)\left[\left(1 - \frac{r^2}{r_N^2}\right)^{1/2} + \frac{1}{\mathcal{L}t}\frac{\sqrt{2}}{3F}\frac{1}{\sqrt{G + \sqrt{G+1}}}\right], \tag{37}$$

$$u = \frac{\dot{r}_N r_N}{r}, \tag{38}$$

where

$$G = (3F\mathcal{L}t)^2\left(1 - \frac{r}{r_N}\right). \tag{39}$$

This solution is illustrated in figure 4.

We comment that the leading order term of this solution, given by

$$h(r,t) = \mathcal{L}r_N(t)\left(1 - \frac{r^2}{r_N^2}\right)^{1/2} \tag{40}$$

is identical to that written down by [16], but this can not be viewed as the complete solution to the shallow layer model because it does not satisfy the dynamic condition at the front (9). Our insight is to show how this leading-order solution emerges as the long time solution of shallow

layer model. At large times, the second term in the composite solution for h is $O((\mathcal{L}t)^{-1})$ close to the current front, consistent with (9), but makes a negligible contribution (of order $(\mathcal{L}t)^{-2}$) to the leading-order lens solution elsewhere. Numerical integration of the shallow layer equations confirms that the composite solution is obtained after the flow has evolved for a sufficient time (figure 4); in terms of the dimensionless variables used here, this requires formally that $\mathcal{L}t \gg 1$. Importantly, this lens solution is rarely fully established for volcanic intrusions in the atmosphere because they are not often sustained for a sufficient duration; this would require a sustained source for a dimensional duration in excess of $1/\Omega \approx 12$ hours. This implies that, for the purpose of predicting the spread of volcanic ash clouds, it is important to compute the time-dependent behaviour *prior* to the establishment of the lens, and a simple way of doing so is presented in the following section.

3. The Coriolis Hybrid model

Although the Coriolis lens solution (40) is established as a solution to the shallow-layer equations when $\mathcal{L}t \gg 1$, our numerical solutions show that the flow at earlier times is quite different (figure 3*a*, *b*). The flow at earlier times exhibits a steady tail from the source to some position $r_1(t)$ (§2.1), at which point it expands through a shock into a thicker annular 'head' with a convex profile (figure 5). The structure of flows with this character was investigated by [14] for non-rotating systems, where it was demonstrated that the flow of sustained radial gravity currents and intrusions may be accurately described by a simplified hybrid model that couples the steady tail with the time evolving head. Here we extend the idea of a hybrid model to the rotating case, in which Coriolis accelerations first influence, and subsequently dominate, the flow behaviour. The extension is not a trivial one because, in the rotating system, the centrifugal and Coriolis accelerations become dominant at sufficiently large radius, producing physical and mathematical complications not present in the non-rotating case.

In particular, it is necessary to consider the azimuthal momentum balance, the fact that the pressure distribution within the head leads to a non-uniform height profile, and the possibility that the propagation will stop (or even change direction) for a while. These features are evident in the numerical solutions of the shallow water equations presented above (§2.2) and guide the development of the hybrid model. We shall demonstrate that the simple hybrid model suggested in this work reproduces these features with reasonable accuracy.

In the hybrid model we assume that, in the domain from the source to some $r_1(t)$, the flow is given by the steady-state solution of the shallow water equations (§2.1), whereas in the domain $r_1(t) \le r \le r_N(t)$, the intrusion is modelled by a truncated lens, as sketched in figure 5. In this latter domain the upper boundary is curved due to Coriolis effects, and the height decreases from $h_J(t)$ to $h_N(t)$. At $r = r_1$ the intrusion expands by a jump from h_1 to h_J. The idea of this model is that the solutions of the shallow-layer equations that are realised are in fact steady in the $r \le r_1(t)$ domain, and an exact solution here is readily available (§2.1). Hence, simplifications are needed only in the $r_1(t) < r \le r_N(t)$ domain. We thus expect that the overall resulting prediction will contain a more reliable physical balance, and be more accurate, than simply using the lens-like solution throughout.

The steady solution analysed in §2.1 (figure 2) provides the form of the hybrid model for $r_i < r_1(t)$. The volume of the steady-state domain is given by

$$\mathcal{V}_1(t) = \int_{r_i}^{r_1} h(r) r \, \mathrm{d}r, \tag{41}$$

using (19), and this is evaluated numerically.

3.1. The head 'box'

We consider now the region $r_1(t) < r < r_N(t)$, where the flow depends on both radius r, and time t, and approximations are needed to obtain a simple model. In the spirit

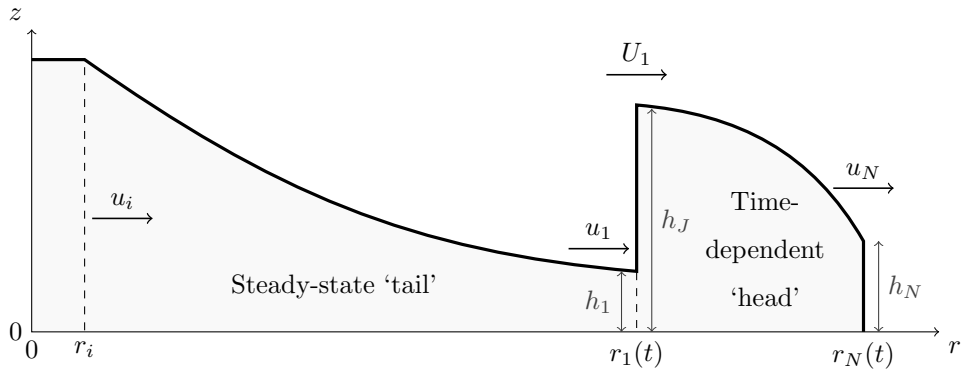

Figure 5: Schematic description of the hybrid model with Coriolis effects.

of box-model approximations, we first define the shape of the control volume under consideration. The inner and outer boundaries are the cylinders r_1 and r_N. The upper interface of our 'box' must be curved, from height h_J to a smaller height h_N, due to the influence of the Coriolis terms; in fact we argue that this domain is dominated by Coriolis. The justification is as follows.

First, we note that the typical radius in this domain is relatively large (even $r > 2$ is sufficient for our arguments). From (14), the angular velocity in the tail for large r is $\omega = -1 + O(r^{-2})$. At the jump, r_1, and inside the head, there are no sources of angular momentum, and hence the angular velocity of a fluid particle also approaches -1. Consequently, the centrifugal-Coriolis term on the right hand side of (3) is, in dimensionless form, $-\mathcal{L}^2 r$ with a relative error $O(r^{-4})$, which is considered negligible. Second, we observe that the inertial terms in the head are small, and decaying with time. In the tail the inertial term $u\partial u/\partial r$ is comparable with the $-\mathcal{L}^2 r$ Coriolis term. At the r_1 jump the intrusion thickens and u is bound to decrease. The speed of the nose, u_N, is also a decaying quantity. While the inertial terms decay, the burden of balancing the centrifugal-Coriolis acceleration in the radial direction over large r is sustained by the pressure gradient $h\partial h/\partial r$. Thus, for calculating the shape of the head domain we use these approximations to simplify the radial momentum balance (3) to

$$\frac{1}{2}\frac{\partial}{\partial r}(h^2) = -\mathcal{L}^2 r, \tag{42}$$

which by integration yields the shape

$$h(r,t) = \mathcal{L}\left[\left(\frac{h_J(t)}{\mathcal{L}}\right)^2 + r_1^2(t) - r^2\right]^{1/2} \qquad (r_1 \le r \le r_N) \tag{43}$$

We note that this simplification in the balance of radial momentum is exactly equivalent to that which is embedded in the asymptotic analysis of §2.3, and thus is the dominant balance in the 'Coriolis lens' solution. This simplification that the depth-integrated pressure (here with a centrifugal correction) has no radial gradient is equivalent to the principle underlying the non-rotating hybrid model of [14]. Given the shape (43), the volume of the head is therefore

$$\begin{aligned}\mathcal{V}_h(t) &= \int_{r_1}^{r_N} hr\,\mathrm{d}r \\ &= \frac{1}{3}\mathcal{L}\left[\left(\frac{h_J}{\mathcal{L}}\right)^3 - \left(\frac{h_J}{\mathcal{L}} + r_1^2 - r_N^2\right)^{3/2}\right].\end{aligned} \tag{44}$$

The first balance equation for the 'box' model is volume continuity:

$$\mathcal{V}_h(t) + \mathcal{V}_1(r_1(t)) = t, \tag{45}$$

where the right hand side is the volume influxed by the source. The combination of (44) and (45) provides an implicit non-linear equation for the height immediately downstream of the jump, $h_J(t)$, as a function of the front

and jump positions, $r_N(t)$ and $r_1(t)$, respectively. We evaluate h_J from this equation with a Newton-Raphson technique, and then use (43) to calculate the height of the nose at $r = r_N(t)$,

$$h_N(t) = \mathcal{L}\left[\left(\frac{h_J(t)}{\mathcal{L}}\right)^2 + r_1^2(t) - r_N^2(t)\right]^{1/2}. \qquad (46)$$

The time-evolution of the head is thus reduced to the task of calculating the evolution of $r_1(t)$ and $r_N(t)$. We recall that r_1 is the position of the jump from the 'tail' to the 'head', and that the conditions u_1 and h_1 at r_{1-} are provided by the steady-state solution (18) and (19) at $r = r_1$. In a frame moving with the speed of the jump, U_1, we write the volume and momentum balances and, after some algebra, obtain

$$\frac{dr_1}{dt} = U_1 = u_1 - \left[\frac{1}{3}\frac{h_J^3}{h_1}(1 + (h_1/h_J)^2 + h_1/h_J)\right]^{1/2}. \quad (47)$$

The jump conditions at r_1 are not directly affected by the Coriolis accelerations, and we use here exactly the same balances as in the non-rotating hybrid model [see 14, Appendix A]. Indirectly, the Coriolis accelerations significantly influence the motion of the jump via the behaviour of h_J in (47). In the non-rotating case U_1 eventually becomes small, but remains positive, and $r_1 \sim t^{3/4}$ for sufficiently large t. In the rotating case the ratio h_J/h_1 becomes, eventually, so large that U_1 changes sign and r_1 shrinks back to the source radius r_i at a finite time t_3, as shown later.

3.2. First stage

For the model to remain physical, the expression inside the square root in (46) must remain positive. In all tested cases this expression is initially positive, but decreases as r_N increases and h_N decreases, and for sufficiently large r_N, h_N reaches zero. We define the 'first stage' as this initial propagation during which $h_N(t) > 0$ and, in this stage, the equation of motion for r_N is provided by the dynamic boundary condition at the front,

$$\frac{\mathrm{d}r_N}{\mathrm{d}t} = \frac{F}{\sqrt{2}}h_N(t). \qquad (48)$$

This closes our formulation (for the first stage) and so, given initial conditions r_1 and r_N at some initial time t_0, we can calculate the subsequent propagation by simple numerical integration of the ODEs (47) and (48) (here we use a 4th order Runge-Kutta method). As by-products of this calculation we obtain the volume of the tail, $\mathcal{V}_1$, and the heights h_J, h_N as functions of t.

The input parameters of the model are $\mathcal{L}$, F and, at the source, r_i, ω_i and either a Froude number or energy condition (12) which together with the mass flux condition $h_i u_i r_i = 1$ specifies both h_i and u_i. In the calculations shown here we use $r_i = h_i = u_i = 1$, $\omega_i = 0$, $F = 1.19$, and study the effect of varying the ratio of rotation rate to stratification $\mathcal{L}$.

It is convenient to start the calculation with $r_N = r_1 = r_i$, and $h_N = h_i$ at $t = 0$. (To achieve a smooth initial adjustment, we add the artificial conditions: if (47) gives a negative value, we change it to $U_1 = 0$; if $U_1 > u_N$, we change it to $0.9u_N$. We emphasise that this condition is applied only in the very initial phase, say $t < 1$, until a physically-valid motion is established. We keep in mind that the details of the matching between the source and the intrusion are not known, and therefore some iterations are necessary to determine the feasible initial conditions for the model. The radius r_N and volume acquired in this initial adjustment have negligible influence on the larger-time flow fields which are our objective.)

The boundary conditions used for our model are compatible with the expected physical behaviour. We obtain that $c_- > 0$ in the steady-state domain $r_i < r < r_1$, which is a necessary condition: this region is dominated by the source, and there is no 'backward' propagation of information from the head. On the other hand, at the nose, and in the head domain, $c_- < 0$; this region is dominated by the front condition. The transition between these two different regions requires the jump at $r_1(t)$. After attaining this qualitative physically-acceptable behaviour, we must consider the quantitative accuracy of the results. This is

assessed by comparisons with solutions of the governing shallow-layer equations, which will be discussed later.

3.3. Second stage

The second stage begins when the height of the front first vanishes ($h_N = 0$), which is accompanied by the arrest of the radial propagation. In the hybrid model we make the approximation that, after this occurs, $h_N \ll h_J$ is maintained thereafter. This approximation is justified by numerical solutions of the full shallow layer model (figure 3), in which the nose height $h_N(t)$ (indicated by crosses) remains very small after the flow front has first stopped, at $t \approx 60$. Substitution of this condition into (46) yields

$$r_N^2(t) = r_1^2(t) + \left(\frac{h_J(t)}{\mathcal{L}}\right)^2, \tag{49}$$

and combining this result with (44) produces

$$\mathcal{V}_h(t) = \frac{\mathcal{L}}{3}\left(\frac{h_J(t)}{\mathcal{L}}\right)^3. \tag{50}$$

Now (45) provides explicitly

$$h_J(t) = \mathcal{L}\left[3(t - \mathcal{V}_1(r_1))/\mathcal{L}\right]^{1/3}. \tag{51}$$

So we observe that the time-dependent solution is determined by the behaviour of $r_1(t)$. The equation of motion for this variable is available: we can use the same governing equation as in the first stage, (47). This is because the jump condition at r_1 reproduces a local balance, which is not affected by the details at the nose r_N which is far away.

This closes our formulation: the second stage begins at $t = t_2$, the end of the first stage, with a known value of r_1. The governing equations are (47), (51), and (49), which replaces the dynamic boundary condition (48). Numerical integration (by the same Runge-Kutta method used for the previous stage) then provides $r_1(t)$, from which the radius r_N, the volume of the nose $\mathcal{V}_1$, and the height h_J can be calculated.

An interesting characteristic of the second stage is that $U_1 < 0$, i.e., the jump moves backwards to the centre. For interpretation we look at (47) and figure 5. When the second stage starts, r_1 has some large value, i.e., u_1 is of order unity and h_1 is small. Since in the second stage r_N expands slowly (or even shrinks), the accumulation of influxed volume increases h_J (see (51)) and applies increasingly backward pressure on the inner side of the head. The ratio h_J^3/h_1 is large, and the second term in the RHS of (47) exceeds the first one. In other words, during the second stage the head recovers the inner annulus which became occupied by the tail in the earlier motion. (We note in passing that the negative U_1 may appear even before the end of the first stage.) This process, however, finishes when r_1 approaches the source radius. To be specific, we define the end of the second phase at $t = t_3$, when $r_1 = 1.1 r_i$. This choice for the transition between phases is of course arbitrary, but with negligible influence on the overall description of motion in the next stage.

3.4. Third stage: the Coriolis lens

At $t = t_3$ the entire influxed volume is in the lens-shaped head, i.e. $r_1 \approx 0$ and $\mathcal{V}_1 = 0$. Substituting these values into (49)–(51) and (43) we obtain exactly the Coriolis lens solution (equations (35) and (40); see also [8] §13.1.1). Because there is no mechanism for changing the underlying Coriolis-pressure balance (we neglect viscous, wind, and instability effects), we argue that this shape will prevail for $t > t_3$.

Thus solutions to our hybrid model approach the Coriolis lens similarity solution at late times, but unlike previous studies that have obtained the Coriolis lens [e.g. 16], we are able to exploit the existence of a steady tail region within the flow at early times to provide an accurate approximation to the flow before the late-time lens solution becomes established.

A peculiarity of the second and third stages of the hybrid model is that r_N varies with t, without apparently being subjected to a boundary condition. The reason for this is that a simplified balance of radial momentum (3) holds in the 'box' region of the second and third stages of

the hybrid model. As we demonstrated in §2.3, when this radial momentum balance holds, the dynamic boundary condition (48) is satisfied by the introduction of a boundary layer is at the front of the flow, causing only a negligible perturbation to the leading-order solution in the bulk of the flow. In the second and third stages of motion, the leading-order location and speed of the flow front can therefore be determined with only a kinematic boundary condition at the front.

4. Results and comparisons

To validate the hybrid model, we compare its predictions to those of the shallow-layer model (details of the shallow-layer computations are given in §2.2). The salient details of propagation, namely the predicted current radius $r_N(t)$ and radial location of the shock $r_1(t)$, are shown in figure 6, for $r_i = h_i = u_i = 1, \omega_i = 0, F = 1.19$ and $\mathcal{L} = 0.01$, 0.05 and 0.1. In general, the qualitative agreement is good, which indicates that the simple model captures well and elucidates the governing physical mechanisms of this complex flow. In particular, we clearly see in the current radius r_N the three stages of motion: expansion of r_N, stopping of the propagation of the flow front, and, after a while, the resumption of growth at a slower rate (figure 6, panels (a) and (c)). The radius r_1 of the tail reaches a maximum towards the end of the first phase, then contracts to the centre (figure 6, panels (b) and (d)).

Solutions of the shallow-layer model exhibit some oscillation in the second stage, while the hybrid model predicts a somewhat smoother behaviour. We note, however, that the amplitude of the oscillations decays with time, and the oscillations are about the line predicted by the hybrid model. At large times both models tend to the Coriolis lens solution.

Figure 7 compares the time t_2 and current radius $r_N(t_2)$ at which the nose of the current first stops (the end of first stage). The hybrid model over-predicts these variables by about 10%, but the dependency of t_2 and $r_N(t_2)$ on $\mathcal{L}$ is

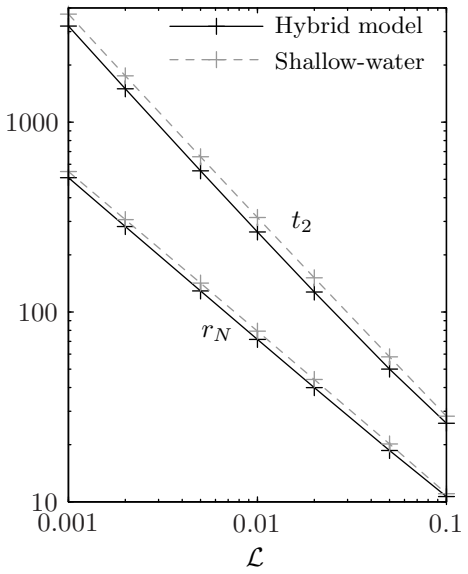

Figure 7: Comparisons of time and current radius at the end of first stage $r_N(t_2)$ and t_2, as functions of $\mathcal{L}$.

in excellent agreement. Roughly, $t_2 = 3/\mathcal{L}$ which is about half-rotation of the system. The corresponding radius is, roughly, $1/\mathcal{L}$ (in dimensional form, $[\mathcal{N}^2 Q/2]^{1/3}/\Omega$). This can be considered the adjustment radius of the intrusion from the initial inertial influx to the situation which is dominated by Coriolis. This can also be regarded as the 'Rossby radius' of the present problem.

The ratio of the current radius $r_N(t)$ predicted by the hybrid model to the prediction $(3t/\mathcal{L})^{1/3}$ of the Coriolis lens is illustrated in figure 8 for various values of $\mathcal{L}$. The time span shown in this figure corresponds to the end of the second stage. The ratio is initially smaller than 1, but attains 1 in a relatively short time interval. There is a significant overshoot at the end of the first stage. The magnitude of the overshoot increases as $\mathcal{L}$ decreases. Then the ratio approaches 1 asymptotically. The occurrence of the peak of the overshot is well correlated with the time $3/\Omega$ (figure 8b), i.e. about one-half revolution of the system; after about 1.5 additional revolutions of the system, the asymptotic value 1 is well approached.

Evidently, the classical $r_N = (3t/\mathcal{L})^{1/3}$ model reproduces the long-time asymptotic behaviour of the system.

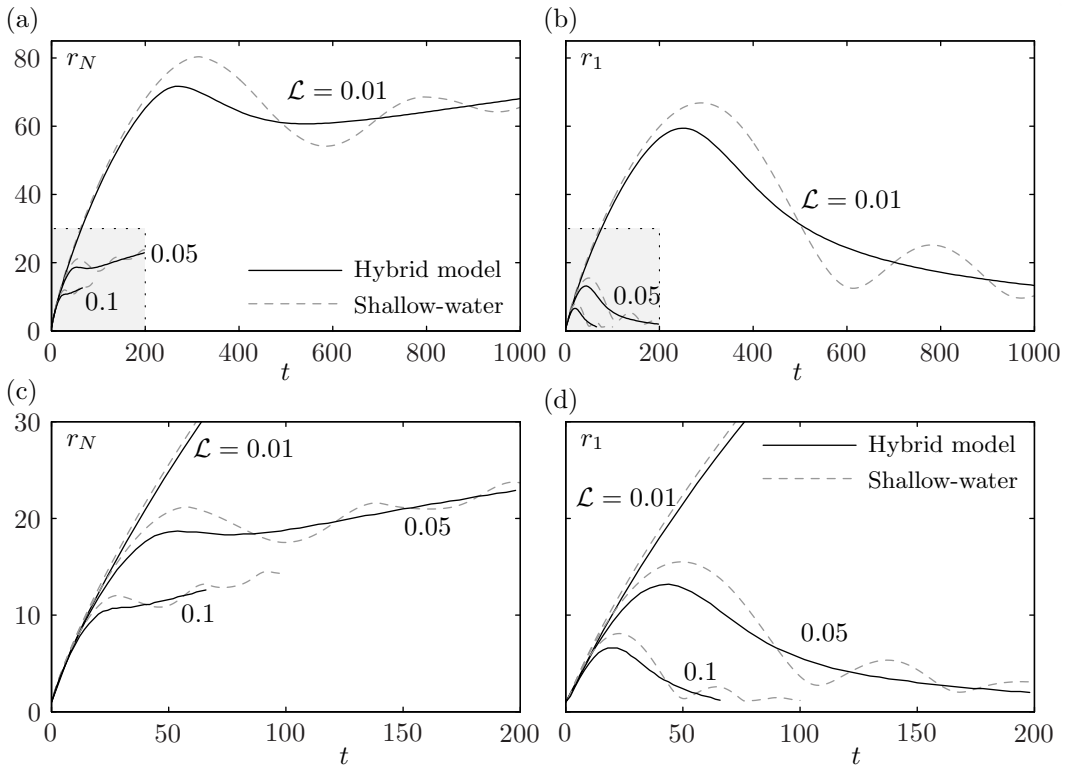

Figure 6: Comparison of current radius r_N (panel (a)), and shock radius r_1 (panel (b)) as predicted by the hybrid model (solid line) and shallow water model (dashed line). Panels (c) and (d) are zooms into the shaded regions of panels (a) and (b), respectively.

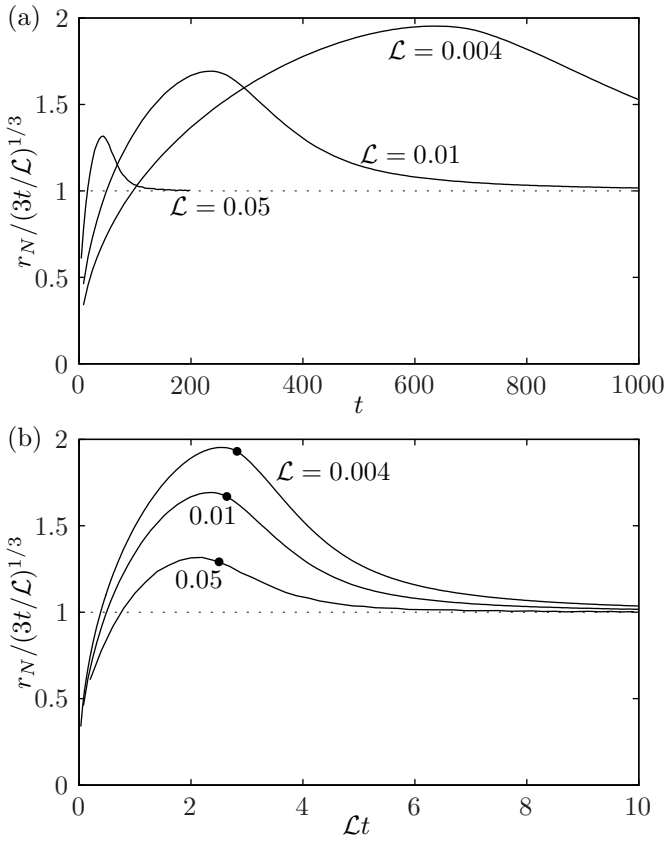

Figure 8: Panel (a): the ratio of the intrusion radius $r_N(t)$ (predicted by the hybrid model) to the radius of the Coriolis lens $(3t/\mathcal{L})^{1/3}$, for $\mathcal{L} = 0.004$, 0.01 and 0.05. Panel (b): the same ratio as in panel (a), plotted against $\mathcal{L}t$, (equivalent to time nondimensionalised with respect to the angular velocity Ω). Dots at $t = t_2$ indicate the end of the first stage of motion.

However, this asymptote is inadequate for the first two stages of propagation of the intrusion (say about two revolutions of the system), and the error is large for small values of $\mathcal{L}$.

5. Conclusions

We have investigated the influence of rotation on the propagation of an axisymmetric intrusion through a stratified ambient created by a constant influx, using a novel hybrid model and accurate numerical solutions of the shallow-layer equations.

The hybrid model reproduces well the propagation of the intrusion both during the initial, inertially-dominated phase, and at later times when Coriolis accelerations influence and subsequently dominate the motion. The model is self-contained, uses no adjustable constants, and requires insignificant computational resources.

We elucidated the following features. The main governing parameter is $\mathcal{L}$, in accord with previously-published investigations, which measures the magnitude of the rotation to the magnitude of the density stratification. We focused attention on cases with small $\mathcal{L}$, relevant to volcanic and other geophysical applications. The propagation has three main stages. In the first stage the inertial forces are important, the steady-state tail expands, but the Coriolis effects achieve dominance in the head, and reduce the speed of propagation to zero. The time at which this occurs is about half a revolution of the system, and the radius of propagation is, roughly, $1/\mathcal{L}$ (in dimensional form, $[\mathcal{N}^2 Q/2]^{1/3}/\Omega$). In the second stage, which extends about one further revolution of the system, the Coriolis-dominated head expands backwards to eliminate the tail; the forward propagation recovers (after possibly a short period in which the front moves inwards).

In the third stage the propagation is $r_N(t) \sim t^{1/3}$, as predicted by the 'naive' inflated-lens model. However, in the first two stages there is significant deviation from this model, in particular a large overshoot at the end of the

first stage (beginning of second stage). This demonstrates the need for, and the advantage of, the more sophisticated hybrid model.

Intuition might suggest that when $\mathcal{L}$ is small, a non-rotating model would suffice for the description of the motion. However, a non-rotating model reproduces the flow with fair accuracy only for the time interval $\mathcal{L}t < 1$, i.e., for about 0.1 revolutions of the system.

The results of our Coriolis hybrid model are supported by the more rigorous predictions of the shallow-layer equations. Needless to say, the shallow-layer model results are more accurate, but the numerical solution of the shallow-layer equations is more computationally expensive than the hybrid model by at least three orders of magnitude, and requires more significant programming effort than the implementation of the hybrid model. A notable difference between the shallow-layer and hybrid model predictions is the more pronounced oscillations of r_N and r_1 predicted by the shallow-layer model. Confirmation of these predictions requires Navier-Stokes simulations and/or laboratory experiments, and this is left for future work, which, we hope, will be motivated and guided by the present paper.

Acknowledgements MU acknowledges the hospitality of the Centre for Geophysical Flows, School of Mathematics, University of Bristol, UK, where a part of this research was performed. AJH and CGJ acknowledge support from EPSRC under grant EP/G066353/1 and from NERC (Natural Environment Research Council) under grant NE/I01554X/1.

[1] R. W. Griffiths, Gravity currents on rotating systems, Ann. Rev. Fluid Mech. 18 (1986) 59–89.

[2] C. J. Lemckert, J. Imberger, Axisymmetric intrusive gravity currents in linearly stratified fluids, J. Hydraul. Eng. ASCE 119 (1993) 662–679.

[3] C. G. Johnson, A. J. Hogg, H. E. Huppert, R. S. J. Sparks, J. C. Phillips, A. J. Slim, M. W. Woodhouse, Modelling intrusions through quiescent and moving ambients, J. Fluid Mech. 771 (2015) 370–406.

[4] T. P. Miller, T. J. Casadevall, Volcanic ash hazards to aviation, in: H. Sigurdsson (Ed.), Encyclopedia of Volcanoes, Academic Press, San Diego, 2000, pp. 915–931.

[5] C. Bonadonna, R. Genco, M. Gouhier, M. Pistolesi, R. Cioni, F. Alfano, A. Hoskuldsson, M. Ripepe, Tephra sedimentation during the 2010 Eyjafjallajökull eruption (Iceland) from deposit, radar, and satellite observations, J. Geophys. Res. 116 (B12).

[6] M. Ungarish, H. E. Huppert, The effects of rotation on axisymmetric particle-driven gravity currents, J. Fluid Mech. 362 (1998) 17–51.

[7] M. A. Hallworth, H. E. Huppert, M. Ungarish, Axisymmetric gravity currents in a rotating system: experimental and numerical investigations, J. Fluid Mech. 447 (2001) 1–29.

[8] M. Ungarish, An introduction to gravity currents and intrusions, Chapman and Hall/CRC, 2009.

[9] A. M. Holdsworth, K. J. Barrett, B. R. Sutherland, Axisymmetric intrusions in two-layer and uniformly stratified environments with and without rotation, Phys. Fluids 24 (3).

[10] K. Hedstrom, L. Armi, An experimental study of homogeneous lenses in a stratified rotating fluid, J. Fluid Mech. 191 (1988) 535–556.

[11] P. G. Baines, R. S. J. Sparks, Dynamics of giant volcanic ash clouds from supervolcanic eruptions, Geophys. Res. Lett. 32 (24).

[12] O. Aubert, M. Le Bars, P. Le Gal, P. S. Marcus, The universal aspect ratio of vortices in rotating stratified flows: experiments and observations, J. Fluid Mech. 706 (2012) 34–45. doi:10.1017/jfm.2012.176.

[13] A. J. Hogg, M. Ungarish, H. E. Huppert, Effects of particle sedimentation and rotation on axisymmetric gravity currents, Phys. Fluids 13 (2001) 3687–3698.

[14] M. Ungarish, C. G. Johnson, A. J. Hogg, A novel hybrid model for the motion of sustained axisymmetric gravity currents and intrusions, European Journal of Mechanics B (Fluids) 49 (2015) 108–120.

[15] J. K. Ansong, B. R. Sutherland, Internal gravity waves generated by convective plumes, J. Fluid Mech. 648 (2010) 405–434.

[16] P. G. Baines, M. T. Jones, R. S. J. Sparks, The variation of large-magnitude volcanic ash cloud formation with source latitude, J. Geophys. Res. 13 (2008) D21204.

[17] R. J. LeVeque, Numerical methods for conservation laws, Vol. 132, Springer, 1992.

[18] R. T. Bonnecaze, H. E. Huppert, J. R. Lister, Particle-driven gravity currents, Journal of Fluid Mechanics 250 (1993) 339–369.

[19] A. Kurganov, E. Tadmor, New high-resolution central schemes for nonlinear conservation laws and convection–diffusion equations, J. Comp. Phys. 160 (2000) 241–282.